

**Marangoni instability of a thin liquid film resting on a locally heated horizontal wall**Leslie Y. Yeo,<sup>1</sup> Richard V. Craster,<sup>2</sup> and Omar K. Matar<sup>1,\*</sup><sup>1</sup>*Department of Chemical Engineering and Chemical Technology, Imperial College London, South Kensington Campus, London SW7 2AZ, United Kingdom*<sup>2</sup>*Department of Mathematics, Imperial College London, South Kensington Campus, London SW7 2AZ, United Kingdom*

(Received 11 October 2002; published 28 May 2003)

Long-wave Marangoni instabilities can be induced thermally on a thin liquid layer overlying a horizontal solid substrate with either a uniform or a nonuniform base temperature. For a nonuniform base temperature, the film height thickens near the region where temperature gradients are negligible and severely thins upstream; “fingering” patterns are observed in this region. These states are related to the patterns observed in the isothermal case, which are reasonably well understood. The stability of these spatiotemporally evolving states to transverse disturbances is investigated using a transient growth-type analysis. It is found that the band of unstable wave numbers exhibiting growth is strongly dependent on the lateral extent of the heating source. Inspection of surface reconstructions of the film thickness profiles reveals the existence of three-dimensional patterns in the thinning region behind the thickened front.

DOI: 10.1103/PhysRevE.67.056315

PACS number(s): 68.15.+e, 47.20.Ma, 68.60.Dv

**I. INTRODUCTION**

Thermocapillary instabilities arise due to nonuniformity in interfacial temperature, resulting in the formation of interfacial tension gradients [1–3]. In thin liquid layers where buoyancy stabilizing mechanisms are negligible, thermocapillary instabilities become dominant, giving rise to tangential stresses at the interface, known as Marangoni stresses, which can induce significant interfacial deformation and possible rupture of the layer.

The study of thermocapillary flows is pertinent to various applications where interfacial flows are encountered, such as in lubricating and coating flows where temperature control is of vital importance in order to impose uniform thicknesses of liquid layers upon solid substrates; any slight variation in the temperature could lead to the growth of instabilities that could disrupt the entire coating layer.

Linear stability theory has commonly been employed to investigate the effect of periodic disturbances on the stability of the thin film. Pearson [4] considered linear stability of pure Marangoni convection on nondeformable interfaces. This analysis was later extended [5] to include deformable interfaces and interfacial tension gradients arising from differences in the surfactant interfacial concentration. While Pearson [4] found that increases in the surface Biot number results in stabilization of the base state, the results of Scriven and Sternling [5] seem to indicate that the system always exhibits long-wave Marangoni instabilities [2], where the characteristic length scale of perturbations is much larger than the thickness of the film layer. However, by allowing for gravity, Smith [6] was able to show that these long-wave instabilities, demonstrated by Scriven and Sternling [5], were suppressed by gravity, thereby reconciling both observations.

Long-wave Marangoni instabilities in thin liquid films

have since been the subject of many investigations [2,3]. They have been observed in various experiments [7–12], where the formation of large scale dry rupture spots was documented. The absence of continuous steady states and spontaneous film rupture due to fingering mechanisms gives rise to new drops, both of which are common characteristics of long-wave Marangoni instabilities; these have also been found numerically. In particular, nonlinear studies have been carried out on horizontal liquid layers [13–15] and falling films [8,12,16–18], as well as for evaporating or condensing films [19]. In addition, the two-dimensional direct numerical simulations of Krishnamoorthy *et al.* [20] on the dynamics of the thinning of horizontal films due to gravitational, capillary, and thermocapillarity effects have shown the formation of structures as the film proceeds toward rupture, similar to those obtained using long-wave theory.

In this paper, we investigate a problem similar to that studied by Boos and Thess [14] and Oron [15] where highly nonlinear effects leading to film rupture were considered. Boos and Thess [14] used the boundary integral method to solve Stokes flow subject to the static and dynamic Bond numbers (defined by  $\rho^* g^* H^{*2} / \gamma^*$  and  $\rho^* g^* H^* / \beta^* \alpha^*$ , respectively, where  $\rho^*$  is the density,  $g^*$  the gravitational acceleration,  $H^*$  the film thickness,  $\gamma^*$  the interfacial tension,  $\beta^*$  the strength of the temperature gradient, and  $\alpha^*$  is the coefficient of interfacial tension variation; the asterisk \* denoting dimensional quantities), and found cascades of large scale to small scale structures close to the onset of rupture. Oron [15], on the other hand, investigated the three-dimensional problem, the solutions of which indicated characteristics borne by the two-dimensional solution.

While Boos and Thess [14] and Oron [15] allow thermocapillarity to arise from surface undulations imposed upon a horizontal liquid layer over a solid substrate of uniform base temperature, we choose to study the more practical case of a system in which the base temperature is initially nonuniform; this case is of current interest and has recently been the subject of experimental investigations by Kabov

\*Corresponding author.

Electronic address: o.matar@imperial.ac.uk

*et al.* [8,12], and modeling work by Miladinova *et al.* [17] and Kalliadasis *et al.* [18] for inclined falling liquid films. Miladinova *et al.* [17] used long-wave theory to conduct a linear, a weakly nonlinear, and a fully nonlinear analysis of the evolution equation governing the film thickness in the presence of thermocapillarity arising from a linear base temperature profile. They found that a positive base temperature gradient is destabilizing with thermocapillarity exerting an influence on the amplitude and phase speed of the finite-amplitude waves. Kalliadasis *et al.* [18], on the other hand, used long-wave theory along with an integral boundary layer (IBL)-type approximation for the energy transport equation to determine a steady film thickness profile for a locally heated falling film. The stability of this nonuniform steady profile to linear transverse disturbances was then conducted and the conditions for instability were determined in terms of a suitably defined Marangoni number for a given lateral extent of the heating source; in the situation considered here we have no steady state.

It is worthy of mention that the thermocapillary instabilities described here are analogous to the Marangoni instabilities that arise out of compositionally driven flows. However, it is often the case that Marangoni instabilities arise from a combination of thermally and compositionally driven flows, such as the classical observation of the “tears of wine” by Thomson [21] where thermal gradients initiate the evaporation of the fluid resulting in concentration gradients, giving rise to Marangoni instabilities. Further work on this phenomenon has been considered recently by Fournier and Cazabat [22], Vuilleumier *et al.* [23], and Hosoi and Bush [24]. In Ref. [24], Marangoni instabilities were observed in the form of longitudinal rolls giving rise to ridge structures near the meniscus. An additional instability was also observed in the form of transverse wave disturbances, earlier discussed by Smith and Davis [25,26]. While Hosoi and Bush [24] considered both thermal and compositional gradients in their stability analysis, they, however, noted that the interfacial motion is driven by compositional rather than thermal gradients as in the case of Vuilleumier *et al.* [23]; the thermal Marangoni number being two orders of magnitude smaller than the compositional Marangoni number. Moreover, the gradients along the streamwise direction were assumed to be much smaller than that in the transverse direction and thus the gradients were only considered in the transverse direction. As such, while the dominant physics are the same in compositionally driven instabilities as they are in their thermally driven counterparts, comparisons between our observations with those in Refs. [23,24] become difficult because of the differing underlying assumptions.

We shall proceed in two parts: First, we examine systems in which the thermal Péclet number,  $Pe$ , is of the order of unity. Here, we use the assumption that the temperature is adiabatically enslaved to the film thickness [15,16,19]; we do not use an IBL approximation such as the one employed by Kalliadasis *et al.* [18]. Subsequently, systems in which  $Pe$  is sufficiently small such that there is a rapid vertical thermal diffusion across the horizontal layer will be studied. In both cases, the nonuniform temperature distribution of the underlying wall leads to severe thinning near the heating source

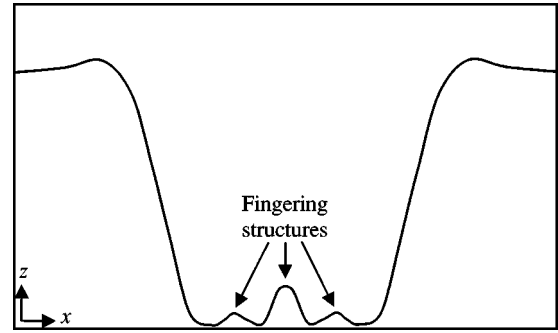


FIG. 1. Schematic illustration of regular fractal-like fingering structures forming in the thinned region behind the thickened outspreading wave front. These patterns are fractal-like in the sense that certain self-similarity in the structures appears to be preserved at increasingly shorter length scales.

and considerable thickening downstream. In the  $Pe \sim O(1)$  case, fractal-like patterns, schematically illustrated in Fig. 1, are observed in the thinning region, similar to those observed previously in the literature [14,15]. The stability of this one-dimensional spatiotemporally evolving base state to applied transverse disturbances is then analyzed using a transient growth-type analysis for a wide range of parameters. Results of this analysis reveal that, for the  $Pe \sim O(1)$  case, this base state could be unstable to disturbances of intermediate wave numbers, which undergo rapid growth prior to the onset of the fractal-like patterns; the stability depends on the lateral extent of the heating source.

The rest of this paper is organized as follows. Section II describes the formulation and treatment of the governing equations together with the relevant initial and boundary conditions; a brief description of the numerical methods used to solve the derived equations is also included. A discussion of the results obtained is then detailed in Sec. III followed by concluding remarks in Sec. IV.

## II. FORMULATION OF THE MATHEMATICAL MODEL

A mathematical description of the physical system, considered, is given in this section. An evolution equation for the height of a thin liquid film resting on a nonuniformly heated solid substrate is derived using lubrication theory for  $Pe \sim O(1)$  in Sec. II A. The film height equation is then linearized using a linear stability analysis. Subsequently, in Sec. II B, we turn our consideration to the formulation and the linearization of the film and temperature evolution equations governing systems in which rapid vertical thermal diffusion is present, that is, where  $Pe \sim O(\epsilon)$ ,  $\epsilon$  being the lubrication parameter which will be defined in Table II. Finally, the relevant initial and boundary conditions are described in Sec. II C and a brief description of the numerical procedures employed to perform simulations of the governing equations is given in Sec. II D.

### A. $Pe \sim O(1)$

#### 1. Derivation of the film evolution equation

A thin film of an incompressible Newtonian liquid with viscosity  $\mu^*$  lying on a planar horizontal solid substrate with

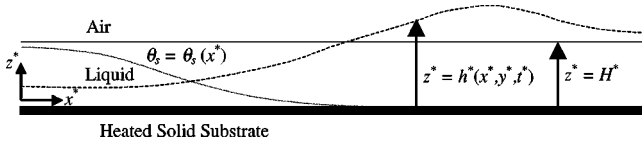


FIG. 2. Schematic representation of the instantaneous height of a thin liquid film,  $h(x, y, t)$  (dashed line), lying upon a nonuniformly heated solid substrate, having a temperature distribution  $\theta_s(x)$  (dotted line); the initial film thickness is  $H^*$  (solid line).

a nonuniform temperature distribution, as shown in Fig. 2, is considered. The initial thickness of the liquid film, of magnitude  $H^*$ , is small in comparison with the lateral extent of the plane,  $L^*$ , such that  $H^* = \epsilon L^*$ , where  $\epsilon \ll 1$ . In such cases, it is possible to assume that standard lubrication theory holds, provided that inertial effects are also small.

We define a spreading pressure  $S^* = \gamma_o^* - \gamma_m^*$ , where  $\gamma_o^*$  and  $\gamma_m^*$  represent the interfacial tension at the free interface of the liquid layer,  $z^* = h^*(x^*, y^*, t^*)$ , corresponding to the region of the minimum and maximum temperatures, respectively; here,  $x^*$ ,  $y^*$ , and  $z^*$  represent the streamwise, transverse, and vertical coordinates, respectively, and  $t^*$  denotes time. These variations in the interfacial tension give rise to Marangoni stresses driving flow in the direction of higher tension [27]. The velocities in the streamwise and transverse planes,  $u^*$  and  $v^*$ , respectively, therefore scale as  $U^* = \epsilon S^* / \mu^*$ , while that in the vertical direction,  $w^*$ , scales as  $\epsilon U^*$ . We can then scale  $x^*$  and  $y^*$  by  $L^*$ ,  $z^*$  by  $H^*$ , and  $t^*$  by  $L^* / U^*$ . The dimensionless interfacial tension  $\gamma$  is given by

$$\gamma \equiv \left( \frac{\gamma_o^* - \gamma_m^*}{\gamma_o^* - \gamma_m^*} \right) = \left( \frac{\gamma_o^* - \gamma_m^*}{S^*} \right), \quad (1)$$

while the dimensionless temperature  $T$  is expressed by

$$T \equiv \left( \frac{T^* - T_\infty^*}{T_m^* - T_\infty^*} \right). \quad (2)$$

In Eq. (2),  $T_m^*$  is the maximum base temperature at the flow origin corresponding to the region of minimum interfacial tension  $\gamma_m^*$ , and  $T_\infty^*$  is the downstream base temperature.

It is convenient at this point to define a linear equation of state relating the interfacial tension to the temperature assuming that the temperature differences are small [1]:

$$\gamma^* = \gamma_o^* + \frac{\partial \gamma^*}{\partial T^*} (T^* - T_\infty^*). \quad (3)$$

Since  $T^* = T_m^*$  when  $\gamma^* = \gamma_m^*$ , the dimensionless equation of state then reads

$$\gamma = 1 - T. \quad (4)$$

Using the above scalings, the dimensionless equation governing the transport of energy can be written as follows:

TABLE I. Typical values for the relevant physical constants for alcohol/water systems.

Physical constant	Symbol	Typical values
Heat capacity	$c_p^*$	$10^3 \text{ J kg}^{-1} \text{ K}^{-1}$
Film thickness	$H^*$	$10^{-5} - 10^{-3} \text{ m}$
Base temperature downstream	$T_\infty^*$	300 K
Spreading pressure	$S^*$	$40 \text{ dyn cm}^{-1}$
Characteristic velocity scale	$U^*$	$10^{-2} \text{ m s}^{-1}$
Air/liquid heat transfer coefficient	$\alpha_h^*$	$10^4 \text{ W m}^{-2} \text{ K}^{-1}$
Liquid/solid heat transfer coefficient	$\alpha_s^*$	$10^2 \text{ W m}^{-2} \text{ K}^{-1}$
Minimum interfacial tension	$\gamma_m^*$	$40 \text{ dyn cm}^{-1}$
Liquid thermal conductivity	$\lambda^*$	$0.1 \text{ W m}^{-1} \text{ K}^{-1}$
Viscosity	$\mu^*$	1 cP
Density	$\rho^*$	$10^3 \text{ kg m}^{-3}$

$$\epsilon \text{Pe} (T_t + u T_x + v T_y + w T_z) = T_{zz} + \epsilon^2 (T_{xx} + T_{yy}) + O(\text{Br}), \quad (5)$$

where the subscripts  $x$ ,  $y$ ,  $z$ , and  $t$  are employed to denote partial derivatives. In Eq. (5), the thermal Péclet number  $\text{Pe}$  is defined by  $\text{Pe} \equiv \epsilon \rho^* c_p^* U^* H^* / \lambda^*$ , where  $c_p^*$  is the heat capacity and  $\lambda^*$  the thermal conductivity of the liquid. Similarly,  $\text{Br}$  is the Brinkman number, defined by  $\text{Br} \equiv \mu^* U^{*2} / \lambda^* T_m^*$ , representing the relative effects of shear heating and thermal conduction.

For typical values of the physical parameters involved (see Tables I and II),  $\text{Br} \sim O(10^{-5})$  and  $\text{Pe} \sim O(1)$ , and thus the dimensionless equation governing the transport of energy in Eq. (5), to leading order, reduces to

$$T_{zz} = 0. \quad (6)$$

At the solid/liquid interface,  $z=0$ , the following boundary condition is imposed:

$$T = \theta_s, \quad (7)$$

TABLE II. Typical values for the relevant dimensionless groups for alcohol/water systems.

Dimensionless group	Symbol	Definition	Typical values
Lubrication parameter	$\epsilon$	$H^* / L^*$	$10^{-2}$
Capillary parameter	$C$	$\epsilon^2 \gamma^* / S^*$	0.001–1
Biot number at liquid/solid interface	$B_s$	$\alpha_s^* H^* / \lambda^*$	0–1
Biot number at air/liquid interface	$B_h$	$\alpha_h^* H^* / \lambda^*$	0–100
Thermal Péclet number	$\text{Pe}$	$\epsilon \rho^* c_p^* U^* H^* / \lambda^*$	$10^{-2} - 1$

where  $\theta_s$  is expressed by

$$\theta_s \equiv \frac{T_w^* - T_\infty^*}{T_m^* - T_\infty^*}, \quad (8)$$

where  $T_m^*$  denotes the temperature at  $z=0$ . Here, we have chosen  $\theta_s = \theta_s(x)$  only. At the free interface,  $z=h$ , where  $h$  is the film thickness, a second boundary condition is imposed:

$$-\lambda^* \frac{\partial T^*}{\partial z^*} = \alpha_h^* (T^* - T_a^*), \quad (9)$$

where  $\alpha_h^*$  denotes the local heat transfer coefficient at the air/liquid interface, and  $T_a^*$  is the temperature at that interface. Defining

$$\theta_h \equiv \frac{T_a^* - T_\infty^*}{T_m^* - T_\infty^*} \quad (10)$$

and

$$B_h = \frac{\alpha_h^* H^*}{\lambda^*}, \quad (11)$$

where  $B_h$  is the surface Biot number, which represents the ratio of the heat transfer rate by convection to that by conduction, the dimensionless form of Eq. (9) can be written as

$$T_z = -B_h(T - \theta_h). \quad (12)$$

Integration of Eq. (6) together with the boundary conditions given by Eqs. (7) and (12) leads to the following temperature profile:

$$T(z) = \frac{B_h \theta_h z + \theta_s + B_h \theta_s (h-z)}{1 + B_h h}. \quad (13)$$

Scaling the pressure  $p^*$  by  $S^*/H^*$ , we can also write the dimensionless equations of mass and momentum conservation, in the lubrication approximation, as

$$u_x + v_y + w_z = 0, \quad (14)$$

$$p_x = u_{zz}, \quad (15)$$

$$p_y = v_{zz}. \quad (16)$$

The normal stress balance at  $z=h$  is given by

$$p = -C(h_{xx} + h_{yy}), \quad (17)$$

where  $C$  is a capillary parameter defined by  $C = \epsilon^2 \gamma_m^*/S^*$ , while a balance of tangential stresses at  $z=h$  reads

$$u_z = \gamma_x + h_x \gamma_z, \quad (18)$$

$$v_z = \gamma_y + h_y \gamma_z. \quad (19)$$

Upon integration of Eqs. (15) and (16), and applying the no-slip and continuity of shear stress boundary conditions at the planes  $z=0$  and  $z=h$ , respectively, we obtain

$$u = \left( \frac{z^2}{2} - zh \right) p_x + zu_z \Big|_{z=h}, \quad (20)$$

$$v = \left( \frac{z^2}{2} - zh \right) p_y + zv_z \Big|_{z=h}. \quad (21)$$

Cross-sectional averaging of Eqs. (20) and (21) over the height of the film, utilizing Eqs. (17)–(19), and making use of Eqs. (4) and (13) yields

$$\begin{aligned} \bar{u} &= \frac{1}{h} \int_0^h u dz = -\frac{h^2}{2} \left[ \frac{B_h h_x (\theta_h - \theta_s) + (1 + B_h h) \theta_{s,x}}{(1 + B_h h)^2} \right] \\ &\quad + \frac{Ch^3}{3} (h_{xxx} + h_{xyy}) \end{aligned} \quad (22)$$

and

$$\bar{v} = \frac{1}{h} \int_0^h v dz = -\frac{h^2}{2} \left[ \frac{B_h h_y (\theta_h - \theta_s)}{(1 + B_h h)^2} \right] + \frac{Ch^3}{3} (h_{xxy} + h_{yyy}). \quad (23)$$

From the kinematic boundary condition,

$$h_t + (h\bar{u})_x + (h\bar{v})_y = 0, \quad (24)$$

the following evolution equation for the film height can be derived:

$$\begin{aligned} h_t &= \left\{ \frac{h^2}{2} \left[ \frac{B_h h_x (\theta_h - \theta_s) + (1 + B_h h) \theta_{s,x}}{(1 + B_h h)^2} \right] \right. \\ &\quad \left. - \frac{Ch^3}{3} (h_{xxx} + h_{xyy}) \right\}_x + \left\{ \frac{h^2}{2} \left[ \frac{B_h h_y (\theta_h - \theta_s)}{(1 + B_h h)^2} \right] \right. \\ &\quad \left. - \frac{Ch^3}{3} (h_{xxy} + h_{yyy}) \right\}_y. \end{aligned} \quad (25)$$

The linearization of Eq. (25) is undertaken next.

## 2. Linearized equations

A small periodic disturbance in the transverse plane is imposed on the film such that the film height can be decomposed into a “base state” component,  $h^{(0)}$ , and a small contribution due to the perturbation with amplitude  $h^{(1)}$ :

$$h(x, y, t) = h^{(0)}(x, t) + h^{(1)}(x, t) e^{ik_y y}, \quad (26)$$

where  $k_y$  is the wave number; it is assumed here that the base flow only varies in the  $x$  direction. It is also assumed in what follows that the temperature of the air,  $T_a^*$ , approaches the base temperature downstream of the flow,  $T_\infty^*$ , such that the simplification  $\theta_h = 0$  may be applied.

By expanding Eq. (25) using Eq. (26), we can decompose the flow in the film into its base state and the corresponding contribution due to the perturbation. Keeping only linear terms in  $h^{(1)}$ , we arrive, for the base state, at

$$h_t^{(0)} = \left\{ \frac{h^{(0)2}}{2(1+B_h h^{(0)})^2} [(1+B_h h^{(0)})\theta_{s_x} - \theta_s B_h h_x^{(0)}] - \frac{Ch^{(0)3}}{3} h_{xxx}^{(0)} \right\}_x. \quad (27)$$

Similarly, we can write for the perturbation,

$$h_t^{(1)} = \left\{ \frac{h^{(0)2}}{2(1+B_h h^{(0)})^2} (B_h h^{(1)}\theta_{s_x} - \theta_s B_h h_x^{(1)}) + \frac{h^{(0)2} h^{(1)}}{(1+B_h h^{(0)})^2} [(1+B_h h^{(0)})\theta_{s_x} - \theta_s B_h h_x^{(0)}] - \frac{h^{(0)2} B_h h^{(1)}}{(1+B_h h^{(0)})^3} [(1+B_h h^{(0)})\theta_{s_x} - \theta_s B_h h_x^{(0)}] - \frac{C}{3} (h^{(0)3} h_{xxx}^{(1)} - h^{(0)3} k_y^2 h_x^{(1)} + 3h^{(0)2} h^{(1)} h_{xxx}^{(0)}) \right\}_x + \frac{B_h \theta_s k_y^2 h^{(0)2} h^{(1)}}{2(1+B_h h^{(0)})^2} - \frac{Ch^{(0)3}}{3} (k_y^4 h^{(1)} - k_y^2 h_{xx}^{(1)}). \quad (28)$$

We note that Eq. (28) is strongly coupled to Eq. (27) and that the dependence of the solution on the derivatives in the  $y$  direction is incorporated into the problem parametrically via the wave number  $k_y$ . Hence, the two-dimensional problem is reduced to a one-dimensional problem.

## B. $Pe \sim O(\epsilon)$

### 1. Derivation of the evolution equations

We now devote our attention to systems in which rapid vertical thermal diffusion is present:  $Pe \sim O(\epsilon)$ , and hence  $\epsilon^2 Pe \ll 1$ . Thus, after  $t \gg O(\epsilon^2 Pe)$ , the temperature in the  $z$  direction equilibrates. Setting  $Pe = \epsilon P$ , where  $P \sim O(1)$ , the dimensionless energy equation given in Eq. (5) becomes

$$\epsilon^2 P (T_t + u T_x + v T_y + w T_z) = T_{zz} + \epsilon^2 (T_{xx} + T_{yy}). \quad (29)$$

We now proceed to decompose the temperature field into a streamwise and transverse component  $T_0(x, y, t)$  and a small fluctuation  $T_1(x, y, z, t)$  which is allowed to depend on  $z$  [28]:

$$T(x, y, z, t) = T_0(x, y, t) + (\epsilon^2 P) T_1(x, y, z, t). \quad (30)$$

Substituting Eq. (30) into Eq. (29), we obtain

$$T_{0t} + u T_{0x} + v T_{0y} = \frac{1}{P} (T_{0xx} + T_{0yy}) + T_{1zz} + O(\epsilon^2). \quad (31)$$

Here,  $T_1$  denotes a fluctuation having a zero cross-sectional average,

$$\bar{T}_1 = \frac{1}{h} \int_0^h T_1(x, y, t) dz = 0. \quad (32)$$

Cross-sectional averaging of Eq. (31) then yields

$$T_{0t} + \bar{u} T_{0x} + \bar{v} T_{0y} = \frac{1}{P} (T_{0xx} + T_{0yy}) + \frac{(T_{1z}|_{z=h} - T_{1z}|_{z=0})}{h}, \quad (33)$$

where  $\bar{u}$  and  $\bar{v}$  represent the cross-sectionally averaged streamwise and transverse velocities, respectively.

The following dimensionless boundary condition is imposed at  $z=0$ :

$$T_z = -B_s (\theta_s - T), \quad (34)$$

where  $B_s$  is the surface Biot number at the solid/liquid interface, defined by

$$B_s = \frac{\alpha_s^* H^*}{\lambda^*}, \quad (35)$$

where  $\alpha_s^*$  is the local heat transfer coefficient at the solid/liquid interface. At  $z=h$ , we have

$$T_z = -B_h (T - \theta_h). \quad (36)$$

Assuming that  $B_s = \epsilon^2 \mathcal{B}_s$  and  $B_h = \epsilon^2 \mathcal{B}_h$ , in which  $(\mathcal{B}_s, \mathcal{B}_h) \sim O(1)$ , we obtain for the flux conditions, upon substitution of Eq. (30) into Eqs. (34) and (36):

$$T_{1z} = -\frac{\mathcal{B}_s}{P} (\theta_s - T_0) + O(\epsilon^2) \quad (37)$$

and

$$T_{1z} = -\frac{\mathcal{B}_h}{P} (T_0 - \theta_h) + O(\epsilon^2). \quad (38)$$

Substitution of Eqs. (37) and (38) into Eq. (33) then yields

$$T_{0t} + \bar{u} T_{0x} + \bar{v} T_{0y} = \frac{1}{P} \left\{ (T_{0xx} + T_{0yy}) + \frac{1}{h} [B_h \theta_h + B_s \theta_s - (B_h + B_s) T_0] \right\} + O(\epsilon^2). \quad (39)$$

From the usual dimensionless equations of motion in the lubrication approximation, together with the normal and tangential stress balances, given by Eqs. (14)–(19), and from Eqs. (4), (20), and (21), decomposition using Eq. (30) and cross-sectional averaging over the film gives

$$\bar{u} = \frac{1}{h} \int_0^h u dz = \frac{C}{3} h^2 (h_{xxx} + h_{xyy}) - \frac{h}{2} T_{0x}, \quad (40)$$

$$\bar{v} = \frac{1}{h} \int_0^h v dz = \frac{C}{3} h^2 (h_{xxy} + h_{yyx}) - \frac{h}{2} T_{0y}. \quad (41)$$

The kinematic boundary condition given by Eq. (24) then yields the film evolution equation:

$$h_t = \left[ \frac{h^2}{2} T_{0x} - \frac{C}{3} h^3 (h_{xxx} + h_{xyy}) \right]_x + \left[ \frac{h^2}{2} T_{0y} - \frac{C}{3} h^3 (h_{xxy} + h_{yyx}) \right]_y. \quad (42)$$

Comparison of Eqs. (25) and (42) in the limit of small  $B_h$  highlights the appearance of a thermocapillary term in the transverse direction, which is absent in Eq. (25). This is due to our choice of  $\theta_s = \theta_s(x)$  only.

### 2. Linearized equations

In the same manner as described in Sec. II A 2, we impose a small periodic disturbance on the film, as described by Eq. (26). In addition, we also impose a similar periodic disturbance on the streamwise and transverse component of temperature as follows:

$$T_0(x, y, t) = T^{(0)}(x, t) + T^{(1)}(x, t) e^{ik_y y}. \quad (43)$$

Expansion of Eqs. (42) and (39) using Eqs. (26) and (43), keeping only linear terms in  $h^{(1)}$  and  $T^{(1)}$ , results in evolution equations for the film and temperature base states as well as their corresponding perturbations.

For the film base state, we arrive at

$$h_t^{(0)} = \frac{1}{2} (h^{(0)2} T_x^{(0)})_x - \frac{C}{3} (h^{(0)3} h_{xxx}^{(0)})_x, \quad (44)$$

whereas the evolution of the film perturbation reads

$$h_t^{(1)} = \frac{1}{2} (h^{(0)2} T_x^{(1)} + 2h^{(0)} T_x^{(0)} h^{(1)})_x - \frac{1}{2} k_y^2 T^{(1)} - \frac{C}{3} \{ [h^{(0)3} (h_{xxx}^{(1)} - k_y^2 h_x^{(1)}) + 3h^{(0)2} h_{xxx}^{(0)} h^{(1)}]_x + h^{(0)3} (k_y^4 h^{(1)} - k_y^2 h_{xx}^{(1)}) \}. \quad (45)$$

Similarly, for the temperature profile, the base state is given as

$$T_t^{(0)} = \frac{h^{(0)}}{2} T_x^{(0)2} - \frac{C}{3} h^{(0)2} h_{xxx}^{(0)} T_x^{(0)} + \frac{1}{\text{P}} \left\{ T_{xx}^{(0)} + \frac{1}{h^{(0)}} [(\mathcal{B}_h \theta_h + \mathcal{B}_s \theta_s) - (\mathcal{B}_h + \mathcal{B}_s) T^{(0)}] \right\} \quad (46)$$

and the perturbation as

$$T_t^{(1)} = h^{(0)} T_x^{(0)} T_x^{(1)} + \frac{h^{(1)}}{2} T_x^{(0)2} - \frac{C}{3} \{ h^{(0)2} h_{xxx}^{(0)} T_x^{(1)} + T_x^{(0)} [h^{(0)2} (h_{xxx}^{(1)} - k_y^2 h_x^{(1)}) + 2h^{(0)} h^{(1)} h_{xxx}^{(0)}] \} + \frac{1}{\text{P}} \left\{ T_{xx}^{(1)} - k_y^2 T^{(1)} - \frac{1}{h^{(0)}} \left[ (\mathcal{B}_h + \mathcal{B}_s) \left( T^{(1)} - T^{(0)} \frac{h^{(1)}}{h^{(0)}} \right) + (\mathcal{B}_h \theta_h + \mathcal{B}_s \theta_s) \frac{h^{(1)}}{h^{(0)}} \right] \right\}. \quad (47)$$

### C. Initial and boundary conditions

The unperturbed thin liquid film is assumed to have a uniform initial thickness,

$$h^{(0)}(x, 0) = 1, \quad (48)$$

and the initial amplitude of the perturbation is assumed to be small and uniform,

$$h^{(1)}(x, 0) = 0.01. \quad (49)$$

For the  $\text{Pe} \sim O(1)$  case, we take

$$T^{(0)}(x, 0) = 0, \quad (50)$$

and a small uniform initial condition for the perturbation,

$$T^{(1)}(x, 0) = 0.01. \quad (51)$$

The relevant boundary conditions are the no-flux conditions at  $x=0$  and  $x=x_\infty$ , where  $x_\infty$  denotes a point downstream, sufficiently far, such that the flow conditions are not influenced by the disturbances caused by the temperature gradients:

$$h_x^{(0)} = h_{xxx}^{(0)} = 0, \quad (52)$$

$$h_x^{(1)} = h_{xxx}^{(1)} = 0. \quad (53)$$

Similarly, for the  $\text{Pe} \sim O(\epsilon)$  case, we assume no-flux conditions at  $x=0$  and  $x=x_\infty$  for the temperature field

$$T_x^{(0)} = 0, \quad (54)$$

$$T_x^{(1)} = 0. \quad (55)$$

We also adopt a Gaussian base temperature profile at the solid/liquid interface,

$$\theta_s = e^{-\alpha(x-x_o)^2}, \quad (56)$$

and at the free interface, we assume

$$\theta_h = 0; \quad (57)$$

$x_o = 0$ , unless otherwise stated. In Eq. (56),  $\alpha$  is a parameter that determines the gradient of the profile.

#### D. Solution methodology

The Method of Lines [29] was adopted for numerical solutions of the full nonlinear one-dimensional film and temperature evolution equations. In the  $Pe \sim O(1)$  case, detailed in Sec. II A, only the film evolution equations for the base flow and perturbation, described by Eqs. (27) and (28), are solved. For the  $Pe \sim O(\epsilon)$  case, detailed in Sec. II B, both the film and the temperature evolution equations are solved, one each for the base state and the perturbation. These equations are described by Eqs. (44) and (45) for the film evolution, and Eqs. (46) and (47) for the temperature evolution, respectively. The solutions are subject to the relevant initial and boundary conditions listed in Sec. II C, i.e., Eqs. (48)–(57). When a uniform base temperature is considered, as will be discussed later, we adopt a cosine disturbance of prescribed wave number as the initial condition.

The spatial derivatives were discretized in the Lagrangian formulation based on a lumped Galerkin–Petrov–Galerkin method, and Gear’s method was used to advance the solution in time [30]. Typically, 2000 grid points were overlaid upon an adaptive grid with a computational spatial domain of up to a maximum length of 50 dimensionless units for times of the order 2000 dimensionless units; convergence was achieved upon mesh refinement. The solutions were also checked for agreement with a separate set of results obtained by integrating the same equations using a partial differential equation solver, PDECOL [31], which is based on the finite element collocation for the discretization of the spatial variable, and the Method of Lines for time integration; 2000 grid points were typically used in the computations for spatial and temporal domains of the same size. In the case of film rupture, the computations were halted when the film thickness became so small such that difficulties arose in resolving accurately the increasingly singular spatial derivatives in the rupture region. The rupture times quoted therefore correspond to the time at which the computations were halted. Additional computations were performed using a spectral code, which utilized 1024 Fourier modes in space and Gear’s method in time over periodic domains, using periodic boundary conditions. Agreement between the results obtained from all numerical procedures was found in all cases.

We have performed simulations using values of the parameters in the following ranges:  $0.001 \leq C \leq 0.1$ ,  $10^{-5} \leq \mathcal{B}_s \leq 10^{-3}$ ,  $0 \leq \mathcal{B}_h \leq 100$ ,  $0 \leq k_x \leq 5$ , and  $10^{-2} \leq P \leq 1$ . For the nonuniform base temperature profile, typically, we use  $\alpha = 0.02$ ; different values for  $\alpha$  will be discussed briefly in the following section.

### III. RESULTS

The presentation of results is organized in the following manner. The results for the  $Pe \sim O(1)$  case are first presented in Sec. III A followed by the results for the  $Pe \sim O(\epsilon)$  case in Sec. III B. In Sec. III A, we present briefly the results for the case of a uniform base temperature in Sec. III A 1. These include linear stability results as well as numerical simulations of film evolution. In Sec. III A 2, we detail results of a transient growth analysis of the time-dependent base state for the case of a nonuniform base temperature, which is aimed at

identifying the band of unstable wave numbers for a given set of parameter values; typical evolution profiles for the base state film height and the height of the superimposed disturbance are also shown. We then proceed to discuss the effect of a variation of the system parameters, namely, the capillary parameter  $C$ , the surface Biot number  $B_h$ , and the wave number  $k_y$  on the growth rate of the disturbances.

#### A. $Pe \sim O(1)$

##### 1. Uniform base temperature

Here, we examine briefly the case of a uniform base temperature,  $\theta_s = 1$ . For an initially uniform film,  $h^{(0)} = 1$ , and a linear perturbation of the form  $h^{(1)} \sim e^{\omega t} e^{(ik_x x + ik_y y)}$ , in which  $\omega$  represents the growth rate of a disturbance having wave numbers  $k_x$  and  $k_y$  in the  $x$  and  $y$  directions, respectively, Eq. (28) reduces to [2]

$$\omega = k^2 \left[ \frac{B_h}{2(1+B_h)^2} - \frac{C}{3} k^2 \right]. \quad (58)$$

Here,  $k^2 = k_x^2 + k_y^2$ , where  $k_x$  and  $k_y$  are the wave numbers in the streamwise and transverse directions, respectively. Positive values of  $\omega$  indicate amplification of the disturbance towards instability whereas negative values indicate decay of the perturbation rendering the system stable in the linear regime. The dispersion relation given by Eq. (58) for various values of the surface Biot number  $B_h$  is illustrated in Fig. 3. It can be seen that there is a critical cutoff wave number,  $k_c = [3B_h/2C(1+B_h)^2]^{1/2}$ , above which the system is always stable [2]. It can also be seen that there is a wave number  $k_m$ , at which the growth rate is maximum, where  $k_m = k_c/\sqrt{2}$ ; this is often referred to as the “most dangerous mode.”

The destabilizing mechanism is fairly well understood: Since the film temperature increases with decreasing thickness, the ‘valleys’ of any surface undulations will be warmer than neighboring ‘hills’ with lower surface tension values. Thermocapillary driven flow will therefore take place from the valleys to the hills, amplifying the amplitude of the undulation and causing instability. This instability is opposed by mean surface tension (capillary) forces, which act to stabilize large wave number disturbances, giving rise to the cutoff wave number mode  $k_c$ . The competition between capillary and thermocapillary forces leads to the existence of a band of unstable wave numbers,  $0 < k < k_c$ , with a well-defined maximum at  $k_m$ .

Figure 3(b) shows the critical cutoff wave number  $k_c$  plotted as a function of  $B_h$ , obtained from Eq. (58) by setting  $\omega = 0$ . Inspection of this figure reveals that  $k_c$  achieves a maximal value at  $B_h = 1$  for all values of  $C$  considered. Moreover,  $k_c \sim B_h^{1/2}$  and  $k_c \sim B_h^{-1/2}$  for  $B_h \ll 1$  and  $B_h \gg 1$ , respectively. This symmetric behavior about  $B_h = 1$ , which can be predicted by differentiating  $k_c$  once with respect to  $B_h$  and setting the result equal to zero, suggests that, in the linear regime, thermocapillarity is particularly destabilizing over an intermediate range of  $B_h$  values. This is due to the fact that for small values of  $B_h$ , thermocapillarity is too weak to am-

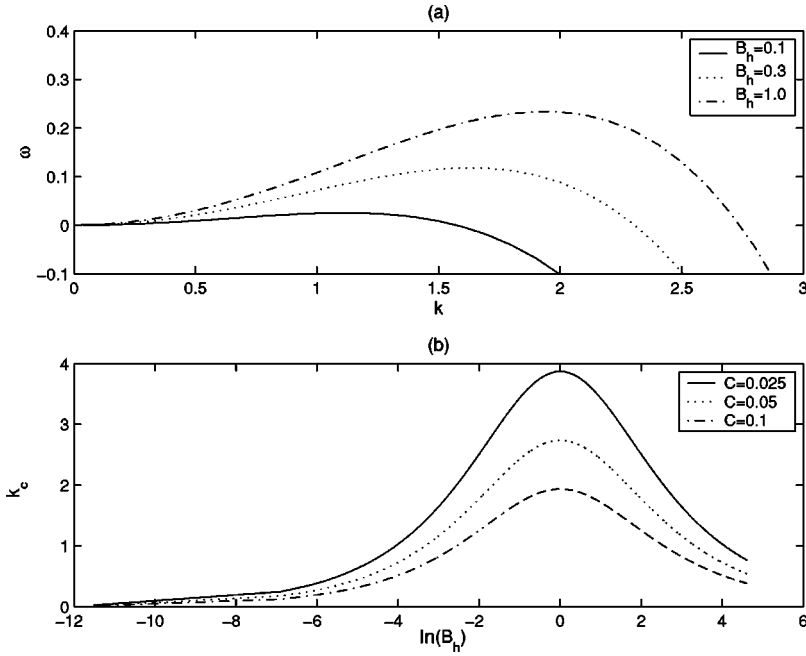


FIG. 3. Linear stability characteristics for the  $Pe \sim O(1)$  case. (a) Growth rate  $\omega$  as a function of the wave number  $k$  for various surface Biot numbers  $B_h$ . The value of the capillary number  $C$  used is 0.05. (b) Neutral stability curves showing the variation of the critical cutoff wave number,  $k_c$ , as a function of the surface Biot number  $B_h$  for various capillary numbers  $C$ .

plify disturbances, while for large  $B_h$  the thermal gradients, which are responsible for instability, are wiped out rapidly (more on this below). Since  $k_c = \sqrt{2}k_m$ , the most dangerous mode  $k_m$  will exhibit almost identical dependence on  $B_h$  to  $k_c$ , except for a constant scaling factor of  $1/\sqrt{2}$ . Finally,  $(k_c, k_m) \sim C^{-1/2}$  indicating that capillary forces are stabilizing for all  $C$ .

It is useful to analyze the effect of local properties, such as the local film thickness, on the linear stability characteristics even though the initial film thickness has been scaled out. To this end, we linearize about  $h^{(0)}$ , a local dimensionless film thickness. Inserting these expressions into those for  $\omega$ , given by Eq. (58), and  $k_m$  yields

$$\omega_l = k_l^2 h^{(0)} \left[ \frac{B_h h^{(0)}}{2(1 + B_h h^{(0)})^2} - \frac{C}{3} h^{(0)2} k_l^2 \right], \quad (59a)$$

and

$$k_{l_m} = \frac{k_{l_c}}{\sqrt{2}} = \frac{1}{2} \sqrt{\frac{3B_h}{Ch^{(0)}(1 + B_h h^{(0)})^2}}, \quad (59b)$$

where  $k_l$  denotes a local wave number and the subscript  $l$  signifies local quantities. These results will be used to explain the behavior of the film undergoing thinning, induced by the underlying nonuniform substrate heating. This will be done by assuming that the quasisteady approximation holds, which will permit linearization about the value of the thickness  $h^{(0)}$ , to which the film will have thinned in a given time. Analysis of the stability of this new base state can then provide information regarding the growth rate and dominant wavelength of perturbations applied to  $h^{(0)}$ . Inspection of Fig. 4, which shows the variation of  $\omega_l$ ,  $k_{l_m}$ , and  $\omega_{l_m} = \omega(k_{l_m})$ , given by Eqs. (59a) and (59b), with  $h^{(0)}$  reveals that  $k_{l_m}$  and  $\omega_{l_m}$  shift to higher values, respectively, as  $h^{(0)}$

decreases. In particular,  $\omega_{l_m}$  and  $k_{l_m}$  tend to the following limiting expressions as  $h^{(0)} \rightarrow 0$ :

$$\omega_{l_m} \rightarrow \frac{3}{16} \frac{B_h^2 h^{(0)}}{C} \quad (60a)$$

and

$$k_{l_m} \rightarrow \frac{1}{2} \sqrt{\frac{3B_h}{Ch^{(0)}}}, \quad (60b)$$

as can be confirmed upon close inspection of Fig. 4. Based on these results, one may tentatively expect that as the film thins in the nonlinear regime to a height  $h^{(0)}$ , the dominant wavelength of the patterns observed shifts to smaller values, since it is proportional to  $h^{(0)1/2}$ , while their growth rate

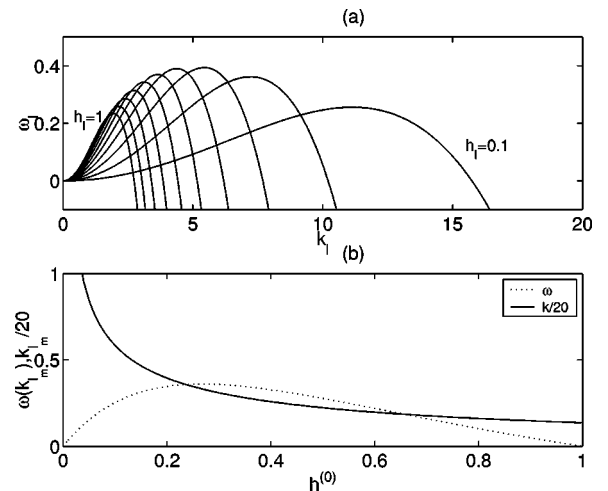


FIG. 4. Linearization about a uniform base state  $h^{(0)}$  for the  $Pe \sim O(1)$  case with  $B_h = 1$  and  $C = 0.05$ . (a) Variation of  $\omega$ , given by Eq. (59a), with  $k$  for  $h^{(0)} = 1.0, 0.5,$  and  $0.25$ . (b) Variation of  $k_m$ , given by Eq. (59b), and  $\omega_m = \omega(k_m)$  with  $h^{(0)}$ .

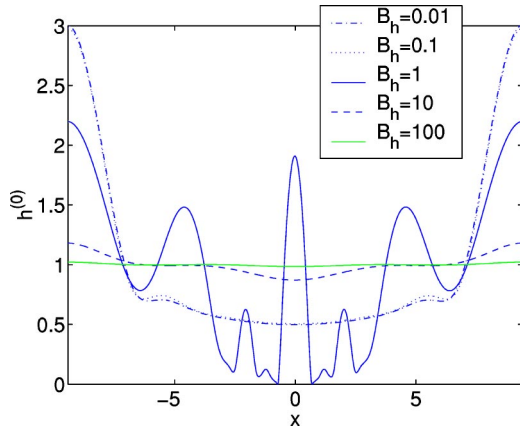


FIG. 5. Profiles of  $h^{(0)}$  at  $t=50$  for various surface Biot numbers,  $B_h$ , for the  $Pe \sim O(1)$  case. The other parameters used in the simulation are  $C=0.05$ ,  $\alpha=0.02$ , and  $k_x=1$ .

decreases. These results will be revisited in the following section, in which the pattern formation accompanying non-uniform film heating is discussed.

Having established the linear stability characteristics of the system, we proceed to solve the one-dimensional nonlinear film height evolution given in Eq. (25), for a uniform base temperature system ( $\theta_s=1$ ), neglecting the transverse  $y$  direction, with the same initial condition used in Ref. [17] to describe a monochromatic wave with a small-amplitude perturbation imposed upon it:

$$h^{(0)}(x,0) = 1 - 0.01 \cos(k_x x). \quad (61)$$

The same boundary conditions used for the nonuniform base temperature case, described by Eqs. (52) and (53), are employed here.

Figure 5 shows the profile of  $h^{(0)}$  at  $t=50$  for the parameters  $C=0.05$  and  $k_x=1$  as a function of the surface Biot number,  $B_h$ . As  $B_h$  is increased, thermocapillary effects be-

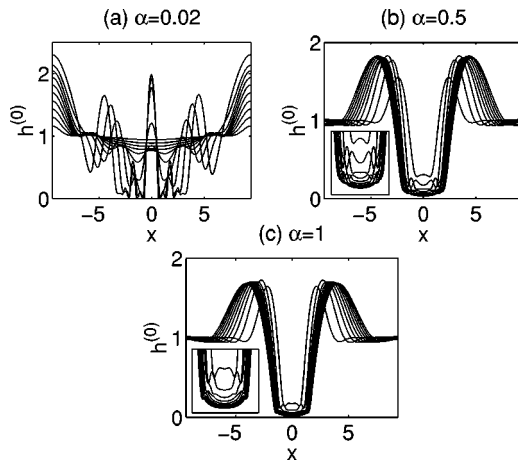


FIG. 6. Evolution of the base state film height with (a)  $\alpha=0.02$ , (b)  $\alpha=0.5$ , and (c)  $\alpha=1$  for the  $Pe \sim O(1)$  case. The rest of the parameters used are  $C=0.05$ ,  $B_h=1$  for ten equal time steps up to  $t=67$ . The insets in (b) and (c) show enlarged views of the thinning region.

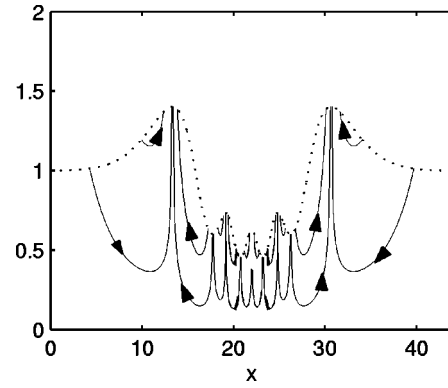


FIG. 7. Streamlines within the film during the formation of the fractal-like structures for  $\alpha=0.02$ ,  $C=0.05$ , and  $B_h=1$  case at  $t=60$ . The dotted line shows the base state film profile at that time.

come increasingly dominant, introducing instability into the system. There is, however, a certain critical value for  $B_h$  at which the growth rate of the disturbance is maximized and hence the instability causes the film to proceed towards rupture; increasing  $B_h$  further beyond this critical value only causes the film to be restabilized. The profiles show an almost symmetric behavior, with the film height for  $B_h=0.1$  almost identical to that for  $B_h=10$ , and  $B_h=0.01$  to that for  $B_h=100$ ; the film appears to be most unstable for  $B_h=1$ . This behavior, exhibited by the film in the nonlinear regime, is in agreement with the predictions of linear theory shown in Fig. 3, in which the neutral stability curve is shown.

For  $\theta_h=0$  and  $\theta_s=1$ , the vertical temperature profile derived in Eq. (13) is reduced to

$$T(z) = 1 - \frac{B_h z}{1 + B_h h^{(0)}}. \quad (62)$$

It can thus be seen that for small or large  $B_h$ , the variation in the liquid film temperature across the film height becomes

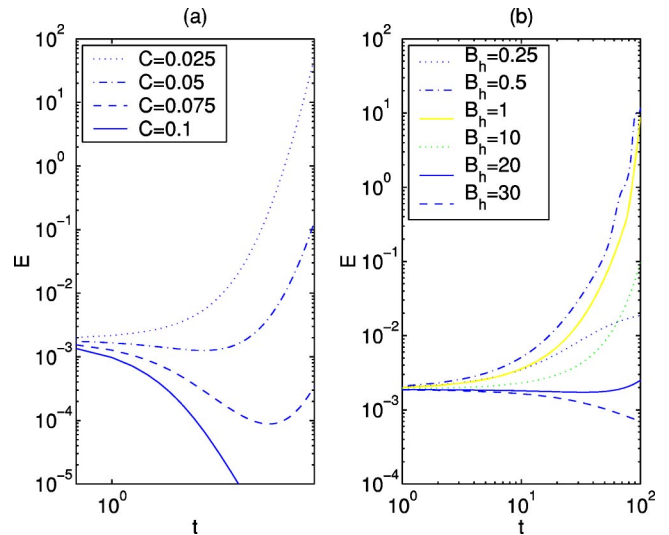


FIG. 8. Growth energy of the disturbance wave,  $E$ , for the  $Pe \sim O(1)$  case. Panel (a) shows the effect of  $C$  with  $B_h=0.25$  and  $k_y=2$ . Panel (b) shows the effect of  $B_h$  with  $C=0.05$  and  $k_y=1$ .

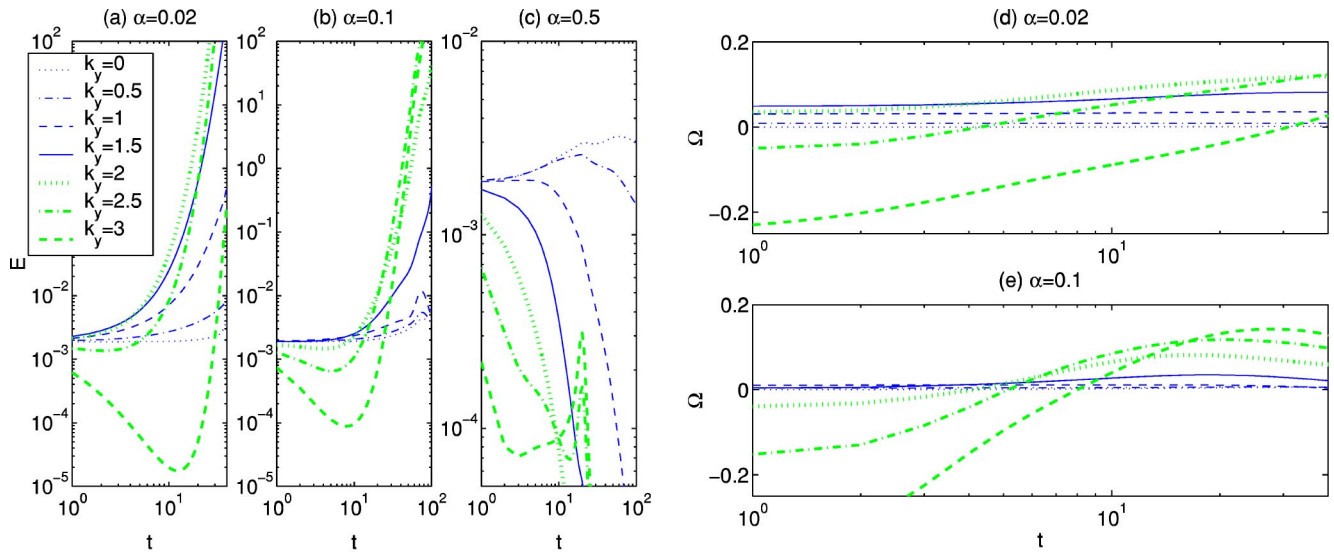


FIG. 9. Temporal variation of  $E$  and  $\Omega$  for various values of the wave number  $k_y$  for the  $Pe \sim O(1)$  case. The rest of the parameter values used are  $C=0.05$  and  $B_h=1$ .

increasingly independent of the height itself due to rapid convection of heat across the height of the film layer. Therefore, for systems in which the thermal conduction is either highly significant or negligibly small compared to the thermal Marangoni convection, surface undulations of small amplitude across the lateral plane are unable to create sufficiently large lateral temperature gradients in order to drive thermocapillary instability. This, therefore, explains the behavior shown in Fig. 5.

The formation of fractal-like fingering structures leading to the creation of dry spots in the local thinning region near the rupture point can also be seen for  $B_h=1$  in Fig. 5; these are similar to the cascade of structures involving the formation of local fingers in the dry-spot region (see Fig. 1) observed by Boos and Thess [14], who solved the Stokes flow problem, and Oron [15], who used standard lubrication theory. In accordance with these studies, we have found no steady-state solution and no simple scaling laws for the minimum rupture thickness during film rupture. The width of the thinning region, however, is governed by the system parameters, in agreement with Boos and Thess [14]. The mechanism for the formation of these cascade structures during film thinning and rupture proposed by Boos and Thess [14] is also evident in our results.

## 2. Nonuniform base temperature

Here, we consider the evolution of the film in the presence of a nonuniform base temperature distribution given by  $\theta_s = e^{-\alpha(x-x_0)^2}$  for the  $Pe \sim O(1)$  case. In what follows, numerical solutions of the nonlinear film evolution equation, Eq. (27), in the absence of a *transverse* disturbance will be termed as “base state” solutions (even though these solutions exhibit an instability in the streamwise direction, as will be shown below). These solutions, denoted by  $h^{(0)}$ , are functions of  $x$  and  $t$ ; no uniform steady base states exist in this case (note, however, that  $h^{(0)}=1$  is a possible base state for linear  $\theta_s$ ). The disturbance  $h^{(1)}$ , on the other hand, which

is also  $x$  and  $t$  dependent, corresponds to a small-amplitude transverse perturbation of prescribed wave number  $k_y$ , imposed upon the base state.

The film profiles for the base state described by Eq. (27) with  $B_h=1$  and  $C=0.05$  can be seen in Fig. 6; the values of  $\alpha$  are taken to be equal to (0.02,0.5,1). This figure demonstrates phenomena that are typical of long-wave Marangoni instabilities. The temperature gradient at the base of the liquid film gives rise to significant thinning near the imposed gradient and thickening downstream, as shown in Fig. 6. Finger-like structures, similar to those observed in Fig. 5 and previous work [14,15], are also evident and appear to be confined to the thinning region, behind the front, which appears to propagate slowly in the streamwise direction. These structures subsequently continue to thin, giving rise to dry spots in the rupture region. The choice of values for  $\alpha$  altered the numerical results qualitatively as well as quantitatively: Steeper temperature gradients corresponding to larger values of  $\alpha$  led to similar formation of the fractal-like structures to those of Fig. 5, but with lower amplitudes. Further increases in  $\alpha$ , however, lead to transient formation of fractal-like peaks in the thinned region; these peaks subsequently flatten out again and disappear, as shown in Figs. 6(b) and 6(c) for  $\alpha=0.5$  and  $\alpha=1$ , respectively. The streamlines at  $t=60$  corresponding to the case of  $\alpha=0.02$  in Fig. 6(a) are shown in Fig. 7. Recirculation regions within the fractal-like peaks can be seen, similar to those found in Ref. [14].

We now proceed to establish connections between the structures observed in Fig. 6 and the long-wavelength thermocapillary instability of a thin film resting on a uniformly heated solid substrate. This is done by considering the local thinning region of the nonuniformly heated substrate case, and comparing its width with the band of unstable wavelengths, as predicted by the linear theory for the isothermal case. Observing that for small values of  $\alpha$  up to  $\approx 0.02$ , the base temperature gradient is small within the local thinning region where the fractal-like structures form behind the front

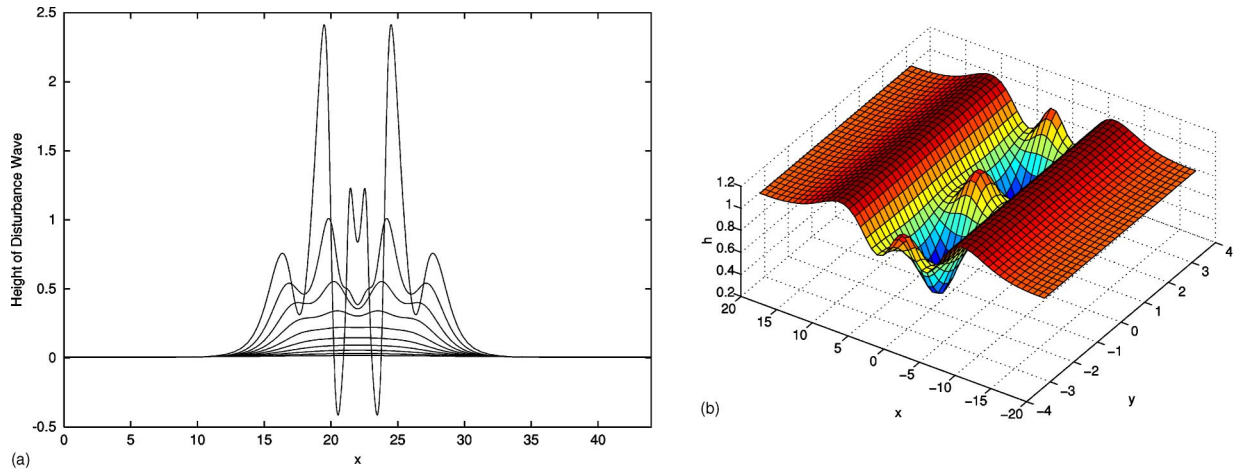


FIG. 10. Two-dimensional evolution profiles of a transverse perturbation of  $k_y = 1$  (a) and a three-dimensional reconstruction (b) of the film height obtained via the superposition of a fraction of the fastest growing mode of the disturbance wave  $k_y = 2$ , with amplitude 0.01, onto the base state film height. Here,  $\alpha = 0.02$ ,  $C = 0.05$ , and  $B_h = 1$ .

of the outspreading wave, thereby permitting such a comparison. It is interesting to note that while the magnitude of  $\alpha$  sets the width of the thinning region in this case, the size of the thinning region in the work of Boos and Thess [14] is governed by all parameters in their system, namely, the static and dynamic Bond numbers, which determine the magnitude of surface tension and thermocapillarity, respectively. In addition, the thinning width is also dependent on the film height and the wave number due to the action of capillarity. An inspection of Figs. 3 and 6(a) indicates that the length of the thinning region, which is approximately ten dimensionless units corresponding to a wave number of  $\pi/5 = 0.63$ , lies within the band of unstable wave numbers predicted by linear theory for the isothermal case. Increasing the temperature gradient (i.e., increasing  $\alpha$ ) makes a similar comparison with linear theory difficult since the quasiisothermal assumption in the thinning region is less valid in this case. The large temperature gradients involved decrease the width of the

thinning region and cause rapid thinning of the film to small values. This thinning, however, is no longer accompanied by fractal, relatively long-wavelength patterns, but rather by wiggles on shorter length scales, as shown in Figs. 6(b) and 6(c), in qualitative agreement with the results given by Eqs. (59) and (60).

We investigate the evolution of applied transverse disturbances next. Increasing  $C$ , such that capillary effects become dominant and counterbalances thermocapillarity, has a stabilizing effect, as shown in Fig. 8 which depicts the energy of the disturbance wave,  $E$  [30]:

$$E = \int_0^\infty h^{(1)2} dx. \tag{63}$$

Although  $E$  decreases initially, for low to moderate values of  $C$  the energy quickly recovers indicating that thermocapillarity becomes the dominant mechanism, driving the onset of instability in the base state and, as a result, causing amplification of transverse disturbances; increasing  $C$  delays the onset of the “recovery” time.

The effect of varying the surface Biot number  $B_h$  is investigated next. Figure 8(b), generated with  $C = 0.05$  and  $k_y = 1$ , shows the dependence of the time-dependent energy curves on  $B_h$ ; rapid growth occurs over intermediate ranges of  $B_h$  values. The applied disturbance decays for  $B_h \leq 0.1$  (not shown). For  $B_h \approx (0.5 - 1)$ , explosive growth occurs and beyond this range, the onset of growth is delayed with increasing  $B_h$ . Finally, for  $B_h \gg 1$ , the disturbance energy undergoes decay in a manner similar to  $B_h \leq 0.1$ . This behavior is reminiscent of that observed in Fig. 3.

Figure 9 illustrates the role of the wave number  $k_y$  on the growth of the disturbance wave. For  $\alpha = 0.02$ , it can be seen from Fig. 9(a) that for very long wavelengths, i.e.,  $k_y \rightarrow 0$ , the disturbance growth is almost constant for a period of time before amplification takes place. Note that even a disturbance having  $k_y = 0$  can be amplified: No translational invariance exists in this system, since  $\theta_s(x) \neq \theta_s(x')$ , where  $x' = x + a$  in which  $a$  corresponds to a small translation in  $x$ ,

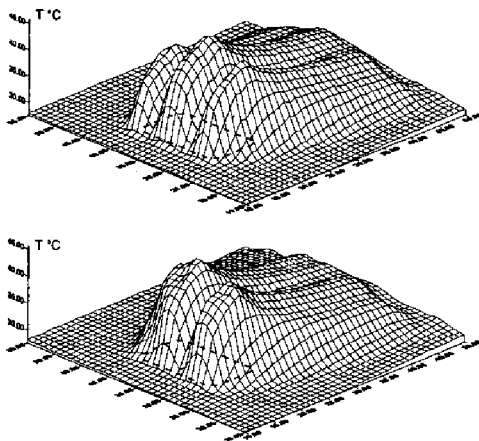


FIG. 11. Three-dimensional infrared image of the liquid film surface in the experiments of Ref. [8], indicating pattern formation in the region of the thickened outspreading wave. The dotted box represents the location of the heater in relation to the observed patterns.

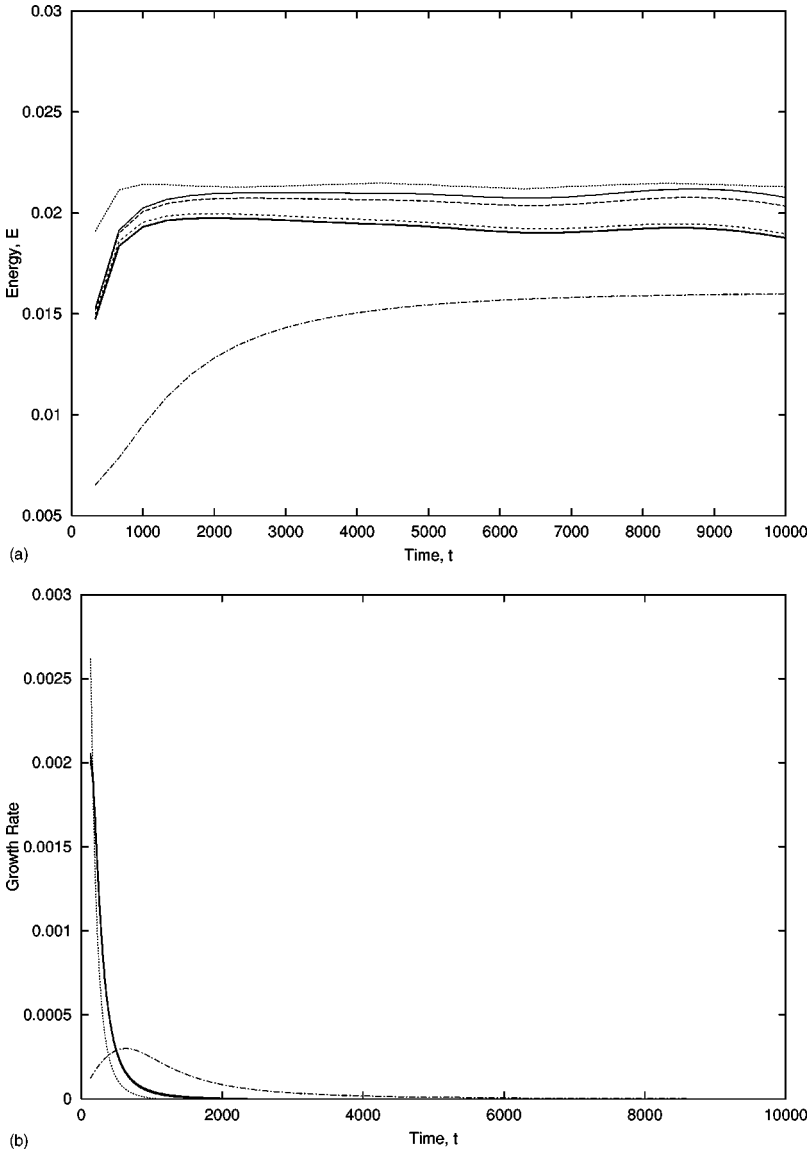


FIG. 12. Temporal variation of  $E$  and  $\Omega$ , shown in (a) and (b), respectively, for various wave numbers  $k_y$ , surface and substrate Biot numbers  $\mathcal{B}_h$  and  $\mathcal{B}_s$ , and thermal Péclet numbers  $P$  for the  $Pe \sim O(\epsilon)$  case with  $x_o=30$  and  $C=0.001$ . The legend is as follows:  $k_y=0$ ,  $\mathcal{B}_h=1$ ,  $\mathcal{B}_s=1$ ,  $P=1$  (—);  $k_y=0.05$ ,  $\mathcal{B}_h=1$ ,  $\mathcal{B}_s=1$ ,  $P=1$  (---);  $k_y=0.1$ ,  $\mathcal{B}_h=1$ ,  $\mathcal{B}_s=1$ ,  $P=1$  (—);  $k_y=0.1$ ,  $\mathcal{B}_h=0.1$ ,  $\mathcal{B}_s=1$ ,  $P=1$  (---);  $k_y=0.1$ ,  $\mathcal{B}_h=1$ ,  $\mathcal{B}_s=0.1$ ,  $P=1$  (—);  $k_y=0.1$ ,  $\mathcal{B}_h=1$ ,  $\mathcal{B}_s=0.1$ ,  $P=3$  (—).

for our choice of  $\theta_s$ ; the equations are, however, translationally invariant for  $\theta_s = 1$ . For shorter wavelengths (larger  $k_y$ ), there is a time period during which the disturbance is suppressed and its energy decays to small values before thermocapillarity becomes dominant resulting in a recovery of the growth rate; this period of time increases with increasing  $k_y$  due to capillary forces, which act to stabilize short wavelength disturbances. For  $k_y$  values intermediate between  $k_y = 0$  and  $k_y = 2.5$ , there is rapid growth in the disturbance leading to instability.

In order to measure the rate of amplification of disturbances, we define the growth rate  $\Omega$  as

$$\Omega = \frac{1}{2E} \frac{dE}{dt}; \quad (64)$$

a discussion of the meaning of stability for time-dependent flow may be found in Ref. [30].  $\Omega$  is plotted parametrically as a function of  $k_y$  with  $\mathcal{B}_h = 1$  and  $C = 0.05$  in Figs. 9(d) and 9(e). An inspection of Fig. 9 reveals that the mode which

initially maximizes the growth rate for  $\alpha = 0.02$  lies in the range  $k_y \in (1, 4)$ . As  $\alpha$  increases the maximal growth rate moves to increasing values of  $k_y$ , as shown in Figs. 9(b) and 9(e). Eventually, for large enough  $\alpha$ , no modes grow substantially, as shown in Fig. 9(c). Thus, we conclude that transverse instabilities are dependent upon the length scale of the thermal forcing; the instabilities also correlate with the severe height variations that occur in the thinning region when  $\alpha$  is small.

Figure 10 depicts the spatiotemporal development of a disturbance of  $k_y = 1$ , which corresponds to the same parameter values as those used to generate Fig. 6(a). Depletion of the liquid film leading to valleys in the base state results in the amplification of the perturbation, up to 300 times its initial amplitude, and the formation of hills, and *vice versa*; this is attributed to the same destabilizing mechanism highlighted earlier. By superimposing a small fraction of the fastest growing mode, here taken to be  $k_y = 2$ , onto the base state of the film, the three-dimensional patterns in the thinned region behind the thickened front can be clearly observed, as shown

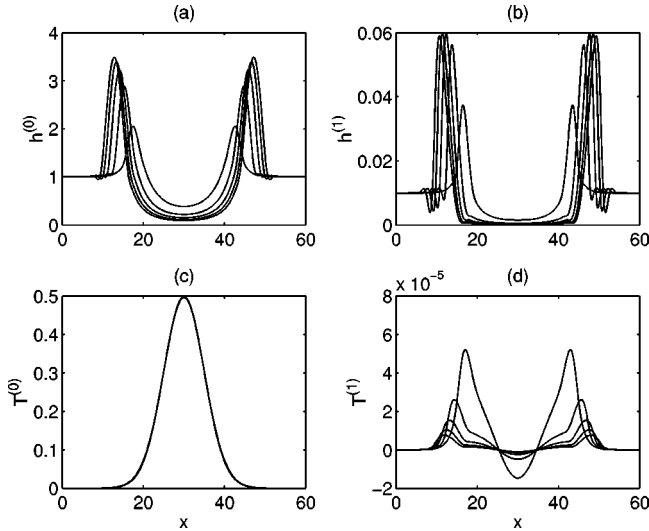


FIG. 13. Evolution of the base state film height (a) and temperature (c), as well as the disturbance wave height (b) and temperature (d) for five equal time steps up to  $t=1000$  for the  $Pe \sim O(\epsilon)$  case. The parameters used are  $x_o=30$ ,  $C=0.001$ ,  $B_s=1$ ,  $B_h=1$ ,  $k_y=0.1$ , and  $P=1$ .

in Fig. 10. These three-dimensional structures become apparent well before the onset of the long-wavelength Marangoni instability, which would have given rise to the fractal-like patterns seen in Fig. 6(a). This transverse instability is therefore expected to dominate the flow in the nonlinear regime. It is worthy of note here that the disturbance is amplified in the thinned region in contrast to the observations of Kabov *et al.* [8,12] and the modeling work of Kalliadasis *et al.* [18] in inclined falling films where the thickened wave front is the target of the disturbance, as shown in Fig. 11. This may be due to the larger convective effects in operation in those cases. In addition, we also note the absence of any transverse wave disturbances in our results, in contrast to the observations of Smith and Davis [25,26], and Hosoi and Bush [24], in spite of carrying out a transient growth analysis that did not preclude the formation of such waves.

### B. $Pe \sim O(\epsilon)$

In the case of rapid vertical thermal diffusion, the long-wave Marangoni instabilities observed previously are no longer apparent over the range of parameters examined. This can be ascertained upon inspection of Fig. 12, which shows the temporal variation of  $E$  and  $\Omega$  as a function of  $B_h$ ,  $B_s$ ,  $P$  and  $k_y$ . Over extremely long periods, the transient growth of the disturbance is seen to stabilize, as observed in Fig. 12(a), followed by decay, as observed in the plot for the growth rate in Fig. 12(b). It should be noted that the capillary numbers used in the simulations are very small such that the stabilizing contribution of capillarity effects over thermocapillary effects are minimized and the chances of instability maximized.

The film thickness and temperature base state and perturbation profiles up to  $t=1000$  are illustrated in Figs. 13(a) and 13(b). The presence of a convecting mechanism drives the

distribution of the temperature perturbation across the entire length of the lateral region so that thermocapillary effects are weakened, as shown in Fig. 13(d). Although it may appear that the amplitude of these perturbations is growing, the energy of all applied perturbations eventually exhibit decay. In addition, the rapid vertical diffusion further results in the dilution of thermocapillary effects. As a result, there is insufficient thermocapillarity to induce long-wave Marangoni instabilities in the system.

## IV. CONCLUSIONS

Long-wave thermocapillary instabilities have been considered for the case of a horizontal thin liquid layer lying upon a solid substrate with both nonuniform and uniform base temperatures. The temperature gradient of the substrate is allowed to drive the thermocapillary action causing the base state to deform into a thickened region downstream of the applied thermal gradient and a thinned region upstream. The latter region becomes unstable to a streamwise rupturing instability. Near the rupture point, fractal-like structures, similar to those observed in Refs. [14,15], for the case of a uniformly heated base are obtained in the thinning region located behind the front of the outspreading wave.

We have carried out a transient growth analysis of these one-dimensional (1D) patterns. A parametric study of the capillary and surface Biot number along with the wave number of the perturbation allows the identification of the “modes” in which the disturbance is amplified and becomes unstable. Capillarity is seen to oppose the destabilizing effect of thermocapillarity by delaying the onset of growth. Analysis of the effects of the surface Biot number, representing the relative magnitudes of thermal Marangoni convection and the heat conducted away from the air/liquid interface of the liquid layer, and the capillary parameter indicated that growth occurs for a range of intermediate Biot numbers.

The formation of the 1D fractal-like structures occurs in a small region, behind the thickened front, in which the base temperature gradient is small; a uniform base temperature within this region can be assumed. By solving for the linearized film evolution equation assuming a constant base temperature and an initially uniform film, the width of the thinning region in the nonuniformly heated substrate case is found to lie within the band of unstable wavelengths, predicted by linear theory for the uniformly heated substrate case. Decreasing the lateral extent of the heating source decreases the width of the thinning region and causes rapid thinning accompanied by the formation of short scale wiggles instead of relatively longer scale fractal-like patterns; this is in qualitative agreement with a local linear stability analysis performed for the isothermal case, which predicts that as the film thins the wavelength of the perturbations is proportional to the square root of the local thickness. As the lateral extent of the heating source decreases the variations in the local temperature field also decrease and the transverse instabilities no longer occur.

In addition, three-dimensional structures were obtained by superimposing a small fraction of the disturbance wave with the fastest growing mode onto the base state film. These

structures in the thinning region are different from those observed experimentally by Kabov *et al.* [8,12] for inclined falling liquid films. In that case, the instability targets the thickened front rather than the thinning region due to the presence of considerable convective effects [18].

By performing a similar transient growth analysis in systems in the limit of rapid vertical thermal diffusion, our results show that the long-wave Marangoni instabilities observed above are diminished. This is due to the thermal gradients being convected along the film interface before

thermocapillary effects become sufficiently dominant to destabilize the film.

#### ACKNOWLEDGMENTS

The authors gratefully acknowledge the assistance of B. Edmonstone and A. S. Patel who participated in the early stages of this work. The authors would also like to thank the EPSRC for funding this work through Grant No. GR/34895.

- 
- [1] S.H. Davis, *Annu. Rev. Fluid Mech.* **19**, 403 (1987).
  - [2] A. Oron, S.H. Davis, and S.G. Bankoff, *Rev. Mod. Phys.* **69**, 931 (1997).
  - [3] M.F. Schatz and G.P. Neitzel, *Annu. Rev. Fluid Mech.* **33**, 93 (2001).
  - [4] J.R.A. Pearson, *J. Fluid Mech.* **4**, 489 (1958).
  - [5] L.E. Scriven and C.V. Sternling, *J. Fluid Mech.* **19**, 321 (1964).
  - [6] K.A. Smith, *J. Fluid Mech.* **24**, 401 (1966).
  - [7] J.P. Burelbach, S.G. Bankoff, and S.H. Davis, *Phys. Fluids A* **2**, 322 (1990).
  - [8] O.A. Kabov, A.V. Diatlov, and I.V. Marchuk, in *Proceedings of the First International Symposium on Two-Phase Flow Modelling and Experimentation, Rome, 1995*, edited by G.P. Celata and R.K. Shah (Edizioni TES, Pisa, 1995), p. 203.
  - [9] S.J. vanHook, M.F. Schatz, W.D. McCormick, J.B. Swift, and H.L. Swinney, *Phys. Rev. Lett.* **75**, 4397 (1995).
  - [10] S.J. vanHook, M.F. Schatz, J.B. Swift, W.D. McCormick, and H.L. Swinney, *J. Fluid Mech.* **345**, 45 (1997).
  - [11] M.F. Schatz, S.J. vanHook, W.D. McCormick, J.B. Swift, and H.L. Swinney, *Phys. Fluids* **11**, 2577 (1999).
  - [12] O.A. Kabov, I.V. Marchuk, A.V. Muzykantov, J.C. Legros, E. Istasse, and J.L. Dewandel, in *Proceedings of the Second International Symposium on Two-Phase Flow Modelling and Experimentation, Pisa, 1999*, edited by G.P. Celata, P.Di. Marco, and R.K. Shah (Edizioni ETS, Pisa, 1999), Vol. 2, p. 1225.
  - [13] A. Oron and P. Rosenau, *J. Fluid Mech.* **273**, 361 (1994).
  - [14] W. Boos and A. Thess, *Phys. Fluids* **11**, 1484 (1999).
  - [15] A. Oron, *Phys. Fluids* **12**, 1633 (2000).
  - [16] S.W. Joo, S.H. Davis, and S.G. Bankoff, *J. Fluid Mech.* **230**, 117 (1991).
  - [17] S. Miladinova, S. Slavtchev, G. Lebon, and J. Legros, *J. Fluid Mech.* **453**, 153 (2002).
  - [18] S. Kalliadasis, A. Kiyashko, and E.A. Demekhin, *J. Fluid Mech.* **475**, 377 (2003).
  - [19] J.P. Burelbach, S.G. Bankoff, and S.H. Davis, *J. Fluid Mech.* **195**, 463 (1988).
  - [20] S. Krishnamoorthy, B. Ramaswamy, and S.W. Joo, *Phys. Fluids* **7**, 2291 (1995).
  - [21] J. Thomson, *Philos. Mag.* **10**, 330 (1855).
  - [22] J.B. Fournier and A.M. Cazabat, *Europhys. Lett.* **20**, 517 (1992).
  - [23] R. Vuilleumier, V. Ego, L. Neltner, and A.M. Cazabat, *Langmuir* **11**, 4117 (1995).
  - [24] A.E. Hosoi and J.W.M. Bush, *J. Fluid Mech.* **442**, 217 (2001).
  - [25] M.K. Smith and S.H. Davis, *J. Fluid Mech.* **132**, 119 (1983).
  - [26] M.K. Smith and S.H. Davis, *J. Fluid Mech.* **132**, 145 (1983).
  - [27] D.A. Edwards, H. Brenner, and D.T. Wasan, *Interfacial Transport Processes and Rheology* (Butterworth-Heinemann, London, 1991).
  - [28] O.E. Jensen and J.B. Grotberg, *Phys. Fluids* **5**, 58 (1993).
  - [29] W.E. Schiesser, *The Numerical Method of Lines* (Academic, San Diego, 1991).
  - [30] O.K. Matar and S.M. Troian, *Phys. Fluids A* **11**, 3232 (1999).
  - [31] N.K. Madsen and R.F. Sincovec, *ACM Trans. Math. Softw.* **5**, 326 (1979).